Bertin *et al. Materials Theory* (2022) 6:1
https://doi.org/10.1186/s41313-021-00031-7

Materials Theory

ORIGINAL ARTICLE Open Access

Sweep-tracing algorithm: in silico slip crystallography and tension-compression asymmetry in BCC metals

Nicolas Bertin* , L.A. Zepeda-Ruiz and V.V. Bulatov

*Correspondence: bertin1@llnl.gov
Lawrence Livermore National Laboratory, Livermore, CA, USA

Abstract

Direct Molecular Dynamics (MD) simulations are being increasingly employed to model dislocation-mediated crystal plasticity with atomic resolution. Thanks to the dislocation extraction algorithm (DXA), dislocation lines can be now accurately detected and positioned in space and their Burgers vector unambiguously identified in silico, while the simulation is being performed. However, DXA extracts static snapshots of dislocation configurations that by themselves present no information on dislocation motion. Referred to as a sweep-tracing algorithm (STA), here we introduce a practical computational method to observe dislocation motion and to accurately quantify its important characteristics such as preferential slip planes (slip crystallography). STA reconnects pairs of successive snapshots extracted by DXA and computes elementary slip facets thus precisely tracing the motion of dislocation segments from one snapshot to the next. As a testbed for our new method, we apply STA to the analysis of dislocation motion in large-scale MD simulations of single crystal plasticity in BCC metals. We observe that, when the crystal is subjected to uniaxial deformation along its [001] axis, dislocation slip predominantly occurs on the {112} maximum resolved shear stress plane under tension, while in compression slip is non-crystallographic (pencil) resulting in asymmetric mechanical response. The marked contrast in the observed slip crystallography is attributed to the twinning/anti-twinning asymmetry of shears in the {112} planes relatively favoring dislocation motion in the twinning sense while hindering dislocations from moving in the anti-twinning directions.

Keywords: Dislocations, Plasticity, MD simulations, BCC, Slip crystallography

Introduction

Understanding metal plasticity from the collective motion of dislocations has been one of the main objectives for materials scientists ever since dislocations were first proposed as the microscopic agents of crystal plasticity. Largely owing to the relentless growth in computing power, direct Molecular Dynamics (MD) simulations were recently demonstrated on previously unattainable length and time scales that are statistically representative of macroscopic single crystal plasticity and yet resolve its fundamental unit mechanisms in all atomistic details (Zepeda-Ruiz et al. 2017, 2021).

The recent surge of interest in large-scale MD simulations of dislocation-mediated plasticity has been greatly facilitated by the dislocation extraction algorithm (DXA) (Stukowski and Albe 2010; Stukowski 2014) that has become instrumental in analyzing the MD data. Given a single atomic configuration (a snapshot) of a crystal, the DXA algorithm detects, locates in space, and determines (indexes) precise Burgers vectors of all dislocations present in the crystal volume. Having already become a classic of computational analysis, the DXA method runs efficiently in parallel and can be performed on the fly during the MD simulation. The classic DXA algorithm provides static snapshots of the dislocation microstructure that, by themselves, provide no quantitative information on the dynamics of dislocation motion. To understand and quantify how dislocations move in a crystal subjected to straining, additional post-processing is required.

In this paper, we introduce a simple and robust algorithm for extracting details of dislocation motion (slip crystallography, dislocation velocities, dislocation flux, etc.) from a sequence of dislocation network snapshots. Although our primary focus here is on dislocation networks extracted by DXA from MD simulations, our new method works equally well on dislocation networks produced in mesoscopic Discrete Dislocation Dynamics (DDD) simulations. Our sweep-tracing algorithm (STA) tracks dislocation motion by reconnecting successive dislocation networks in a way that is independent of the details of line discretization and agnostic to the network topology. The key idea of the method is to circumvent the difficult problem of matching the topology of two successive dislocation networks by representing the same line networks as configurations of the dislocation density (Nye's) tensor field on a spatial grid. Using such a dual representation – line and field – the task of tracing dislocations motion is transformed into an optimization problem that seeks to minimize a distance between pairs of successive dislocation networks. During this process, STA reconstructs details of dislocation motion in the form of slip facets reconnecting dislocation line segments in two successive network snapshots, thereby allowing to extract quantitative information on dislocation dynamics.

In "The sweep-tracing algorithm (STA)" section, we introduce the STA method and discuss its algorithmic implementation. In "Results" section, STA is used first to analyze the motion of dislocations produced by expansion of a single dislocation loop and then applied to large scale simulations of dislocation-mediated plasticity in body-centered cubic (BCC) tantalum subjected to uniaxial tension and compression. The resulting STA data is then discussed in "Discussion and conclusion" section where the notorious tension/compression asymmetry of the flow stress response in BCC metals is related to a distinctly different crystallography of dislocation slip observed in silico under tension and compression.

The sweep-tracing algorithm (STA)

In principle, human eye is efficient in grasping essential characteristics of dislocation motion by reconnecting together positions and orientations of individual line segments attained in successive network configurations. While instructive and entertaining, visual analysis is often inefficient in collecting quantitative statistical data and, at times, deceptive in attempting to quantify how the dislocations move. Here we seek to develop a quantitative analog of "visual tracking" in which two successive snapshots of a dislocation network at times t and $t + \Delta t$ are reconnected in a non-arbitrary quantitative way.

Although the task may present itself as trivial at a first glance, several practical difficulties arise when trying to reconnect dislocation networks.

First, the two snapshots need to be sufficiently close apart in time for any reconnection to be possible and to remain unambiguous. Conversely, when two successive network configuration are too far apart, essential details of dislocation motion can be lost making it impossible to unambiguously reconnect two configurations. Even though STA can reconnect any two network configurations, however distant, in the following we will implicitly assume that Δt is sufficiently small so that, from one frame to the next, dislocations move over distances smaller than the mean dislocation spacing.

The second difficulty is that dislocation networks change their topology such as when dislocations intersect and zip into junctions, or when the junctions break apart or when line discretization is refined or coarsened from one time instance to the next. In DXA, changes in network topology can be observed even on the time scale of a single simulation time step, e.g. owing to incessant thermal vibrations of the atoms. This means that, when considered as two graphs, successive networks extracted via DXA analysis are generally *nonisomorphic*, thereby precluding the use of direct graph matching procedures.

It should still be possible to quantify dislocation motion by matching segments that belong to the maximum common sub-graph even when two dislocation network graphs are nonisomorphic. Provided Δt is sufficiently small, uncommon remainders of two graphs should be small and can be excluded from statistical analyses. However, numerical algorithms for computing the maximum common sub-graph of two graphs are known to be NP-complete in computational complexity (Garey and Johnson 1979) rendering such calculations practically unfeasible for networks containing more than 10^4 physical nodes (such network sizes are now routinely achieved in large-scale MD simulations of crystal plasticity (Zepeda-Ruiz et al. 2017, 2021)).

To overcome the difficulties outlined above, the key idea of the STA method is to first convert each dislocation line network into a continuous field accurately representing the network's geometry and Burgers vector charges, and then reconnect two dislocation networks by matching their field representations. Among several known continuum field representations, we use the Nye's tensor (also known as dislocation density) field (Nye 1953) to represent the dislocations networks. For our purposes here it is sufficient to define the continuous dislocation fields on a regular grid. If desired, the grid can be selected to have the same geometry as the underlying crystal lattice (body-centered cubic in tantalum). Here for simplicity we define dislocation density fields on a simple cubic grid.

Consider a dislocation network $\mathcal{N}$. The Nye's tensor $\boldsymbol{\alpha}^{\mathcal{N}}(\boldsymbol{x})$ at every field point $\boldsymbol{x}$ due to the presence of dislocation lines that constitute dislocation network $\mathcal{N}$ is

$$\boldsymbol{\alpha}^{\mathcal{N}}(\boldsymbol{x}) = \int_{\mathcal{N}} \boldsymbol{b}(\boldsymbol{x}') \otimes \boldsymbol{t}(\boldsymbol{x}')\delta(\boldsymbol{x} - \boldsymbol{x}')\, dl(\boldsymbol{x}') \tag{1}$$

where integration is performed along dislocation line segments of the network $\mathcal{N}$. Here, $\boldsymbol{b}$ is the Burgers vector, $\boldsymbol{t}$ is the unit tangent vector of the line, and $\delta(\boldsymbol{x})$ is the Dirac delta function. As written above, the Nye's tensor is non-zero only in field points lying on the line segments of dislocation network $\mathcal{N}$, however the Nye's tensor content in any given material volume can be computed as a line integral over the network segments inside the same volume. Numerically, the singular Nye's tensor field $\boldsymbol{\alpha}^{\mathcal{N}}\left(\boldsymbol{x}^d\right)$ of an arbitrary dis-

location network can be approximated on a discrete spatial grid $\Omega^d = \{\boldsymbol{x}^d\}$ so that its volume content on the grid points is preserved. Here we use an analytical partition of unity method *to smear out* the singular Nye's tensor of a line dislocation network over a regular grid. As shown in (Bertin 2019), such network-to-field mapping is robust and easy to compute. And, while agnostic to network topology and to specific line discretizations employed in DXA and DDD models, the resulting field can approximate an arbitrary dislocation line network to any desired accuracy using appropriately small grid spacing.

As a measure of distance between two dislocation networks $\mathcal{N}_1$ and $\mathcal{N}_2$ represented by two fields $\alpha_{ij}^{\mathcal{N}_1}\left(\boldsymbol{x}^d\right)$ and $\alpha_{ij}^{\mathcal{N}_2}\left(\boldsymbol{x}^d\right)$, we use the following metric

$$E(\mathcal{N}_1,\mathcal{N}_2) = \sum_{\Omega^d}\sum_{ij}\left(\alpha_{ij}^{\mathcal{N}_1}\left(\boldsymbol{x}^d\right) - \alpha_{ij}^{\mathcal{N}_2}\left(\boldsymbol{x}^d\right)\right)^2 \tag{2}$$

where $i,j = \{1,2,3\}$ are the indices of the Nye's tensor components and the external sum runs over all grid points. The superscripts indicate that two Nye's tensor fields are on-the-grid representations of two dislocation line networks $\mathcal{N}_1$ and $\mathcal{N}_2$.

Consider now two successive dislocation networks $\mathcal{N}_t$ and $\mathcal{N}_{t+\Delta t}$ extracted from snapshots taken at time t and $t+\Delta t$, respectively. To reconnect the two networks let us now deform network $\mathcal{N}_t$ so as to match its Nye's tensor field $\alpha_{ij}^{\mathcal{N}_t}\left(\boldsymbol{x}^d\right)$ as closely as possible to the Nye's tensor field $\alpha_{ij}^{\mathcal{N}_{t+\Delta t}}\left(\boldsymbol{x}^d\right)$ of network $\mathcal{N}_{t+\Delta t}$. Here by network deformation we mean an arbitrary distortion of network geometry (moving network nodes and segments around) without changing network topology (which segments connect which nodes). This trick of *isotopological* deformation is intended to find a deformed earlier network $\tilde{\mathcal{N}}_{t+\Delta t}$ as a best geometric approximant of the later network $\mathcal{N}_{t+\Delta t}$ while maintaining the original topology of network $\mathcal{N}_t$. Best matching can be achieved by deforming network $\tilde{\mathcal{N}}_{t+\Delta t}$ so as to minimize its on-the-grid distance to network $\mathcal{N}_{t+\Delta t}$. Minimization of the distance metric function is performed with respect to positions $\{\boldsymbol{r}\}$ of all nodes of the deformed network $\tilde{\mathcal{N}}_{t+\Delta t}$ using an appropriate numerical method, e.g. gradient-descent. If needed the grid can be adaptively refined to achieve closer matching. More details on the numerical implementation of the algorithm are provided in Appendix A.

Given that networks $\mathcal{N}_t$ and $\tilde{\mathcal{N}}_{t+\Delta t}$ have the same topology by construction, incremental motion of each line segment of network $\mathcal{N}_t$ can be unambiguously traced by connecting two end nodes of each segment in $\mathcal{N}_t$ to the corresponding end nodes of the same segments in the deformed network $\tilde{\mathcal{N}}_{t+\Delta t}$. As illustrated on Fig. 1a, the quadrilateral with two edges coinciding with two positions of the same line segment in $\mathcal{N}_t$ and $\tilde{\mathcal{N}}_{t+\Delta t}$ and two other edges connecting (tracing) its end nodes, defines a unit slip facet. In addition to the Burgers vector $\boldsymbol{b}^i$ of its line segment, each slip facet i is assigned vector $\Delta\boldsymbol{A}^i$ of magnitude equal to the area swept by the segment over time interval from t and $t+\Delta t$ and of direction normal to the plane in which the segment glides over the same time interval. Thus, contribution of each slip facet to the net plastic distortion of the crystal is $\Delta\boldsymbol{\gamma}^i = \Delta\boldsymbol{A}^i \otimes \boldsymbol{b}^i/V$, where V is the crystal volume. As defined, the slip facets are not necessarily flat, but their $\Delta\boldsymbol{A}^i$ vectors can be approximated as cross-products of two facet diagonal vectors, as depicted in Fig. 1a. Excessive "warpage" of any such slip facet is an indication that time interval Δt and/or grid spacing are probably too large. Optimal values of Δt and grid spacing are defined by user's demands on accuracy and available computational resources. More details on the choice of the STA parameters and on the validation of the approach by comparing to DDD data are presented in Appendix B.

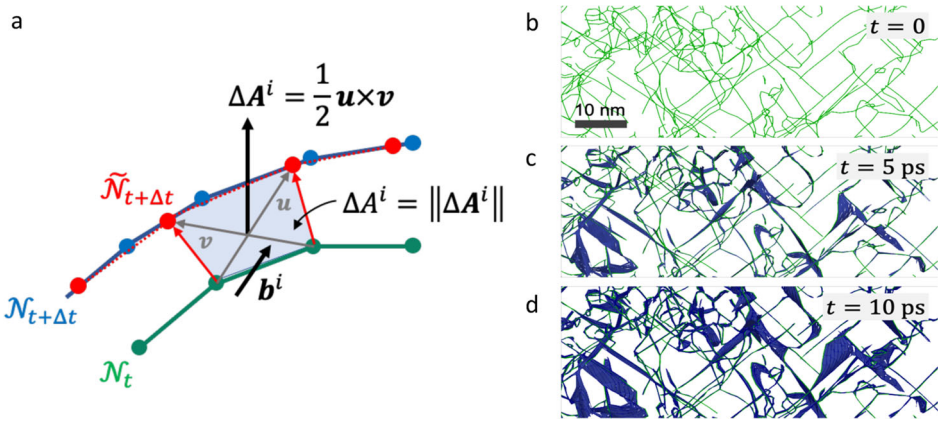

Fig. 1 **a** Schematic of a unit slip facet $(\Delta \boldsymbol{A}^i, \boldsymbol{b}^i)$ (shaded quadrilateral) extracted with the STA algorithm by reconnecting networks $\boldsymbol{\mathcal{N}}_t$ (green nodes and segments) and $\boldsymbol{\mathcal{N}}_{t+\Delta t}$ (blue nodes and segments) through approximant $\widetilde{\boldsymbol{\mathcal{N}}}_{t+\Delta t}$ (red nodes and dashed red segments). The magnitude $\Delta A^i = \|\Delta \boldsymbol{A}^i\|$ of the normal vector is equal to the area swept by the segment over the same time interval Δt. (**b**–**d**) Dislocation motion in the form of slip facets extracted using the STA algorithm from an MD simulation of metal plasticity in bcc Ta. **b** The green lines show dislocation positions at time $t = 0$. The blue surfaces are composed of slip facets reconnecting positions of the same dislocations at **c** $t = 5$ps and **d** $t = 10$ps

Figure 1b-c is an example of slip facets obtained as the output of the STA algorithm applied to a series of successive dislocation networks extracted from an MD simulation of metal plasticity in tantalum. Another example of STA output is presented in Supplementary Movies 1-3.

Results

MD simulations setting

As a case study we applied STA algorithm to DXA data extracted from MD simulations of tantalum single crystals. In this section we use STA analyses to establish if and how two hallmark phenomena of crystal plasticity in BCC metals, namely the notorious tension/compression (T/C) asymmetry and its related phenomenon of twinning/antitwinning (T/AT) asymmetry, manifest themselves in crystallography of dislocation motion. MD simulations reported here were performed on small fragments of the BCC lattice seamlessly embedded into an infinite crystal using 3D periodic boundary conditions using the open source code LAMMPS (Plimpton 1995). The crystals were created with atoms arranged in orthorhombic periodic supercells with repeat vectors aligned along the cube axes of the BCC lattice. Dislocations were seeded into the crystal in the form of hexagon-shaped prismatic loops of the vacancy type after which the model crystals were equilibrated at 300K under zero pressure. The crystals were then subjected to uniaxial deformation along the [001] direction at a 'true' strain rate of $\dot{\varepsilon} = 2 \times 10^8$/s while maintaining the ambient conditions using an appropriate barostat and a thermostat. Poisson expansion (under compression) and contraction (under tension) were enabled resulting in a pure uniaxial stress state. To model the inter-atomic interactions in tantalum we employed a well known EAM potential developed by Li et al. (Li et al. 2003). During the simulations, dislocation networks were extracted on-the-fly every $\Delta t = 1$ ps apart using the DXA algorithm (Stukowski 2014). The so-extracted dislocation network snapshots were then reconnected using the STA algorithm thus providing statistical data for further analyses.

Tension / compression asymmetry in single-loop simulations

We first examine the case of a single prismatic loop subjected to compression or tension. A hexagon-shaped prismatic loop of 15 nm radius of the vacancy type with Burgers vector $\frac{1}{2}[\,111]$ was initially carved out near the center of a cubic simulation cell with side-length 66 nm containing about 16 million atoms. The three pairs of opposite edges of the hexagon were aligned with three $\langle 112\rangle$ directions of the [111] zone. Once relaxed, the edges formed three pairs of pure edge dislocations, each pair lying on one of the three {110} planes of the [111] zone. Of our primary interest here is the still unresolved issue of slip crystallography (Weinberger et al. 2013), namely in which planes the dislocations glide (or slip) while producing plastic strain in BCC metals.

As discussed in (Duesbery and Vitek 1998; Ito and Vitek 2001; Vitek 2004; Dezerald et al. 2016), at its base the tension/compression asymmetry in BCC metals originates in a geometric twinning/anti-twinning (T/AT) asymmetry of crystallographic slip in the planes of the $\langle 111\rangle$ zones. It is straightforward to observe that, for all shear planes of the $\langle 111\rangle$ zone except {110}, the change in relative positions of atoms induced by a small shear displacement along the densely packed $\langle 111\rangle$ directions depends not only on the magnitude of the shear displacement but also on its sign: shearing along a $\langle 111\rangle$ direction in the twinning (T) direction meets less resistance that shearing along the same slip vector in the opposite anti-twinning (AT) direction. This rather basic geometric asymmetry is the reason why deformation twins in BCC metals nucleate and grow only in the sense of twinning shear but never as anti-twins. The same geometric asymmetry translates into a markedly higher resistance (e.g. Peierls stress) to dislocation motion in the {112} planes sheared in the AT direction than to the motion of the same dislocations under shear in the T direction. The T/AT asymmetry affects resistance to motion of dislocations of all characters in all planes other than {110}.

For a more detailed analysis of T/AT asymmetry on slip crystallography, rather than dealing with planar shears and stress (which are tensors), its convenient to consider displacements of and Peach-Koehler forces on screw dislocations. As illustrated in Fig. 2, when a BCC crystal is strained along its [001] axis, the PK force acting on a screw $\frac{1}{2}[\,111]$ dislocation is parallel to the vertical $(11\bar{2})$ slip plane often referred to in the literature as the maximum resolved shear stress plane (MRSSP). In the specific frame of Fig. 2, the PK force acting on a right-hand screw dislocation points downward under [001] compression and upward under [001] tension (the PK force on a left-hand screw will point in the opposite directions). We can now use slip facets extracted from a sequence of DXA snapshots to observe in which planes the dislocations prefer to move.

Figure 3a–b show dislocation configurations attained after straining the crystal over time $t = 200$ ps under compression (a) and under tension (b). Although two configurations are clearly different, it is hardly possible to tell visually from the static snapshots how the dislocation motion contributed to their differences. To understand and quantify differences in slip crystallography, we use STA facets computed on the sequences of dislocation networks extracted from two MD trajectories using the DXA method. Figure 3 uses two different ways to display slip facet statistics. Shown in Fig. 3c–f are the integral statistics of slip facet normals computed on every pair of DXA dislocation networks extracted at intervals 1 ps and accumulated over time from $t = 0$ to $t = 400$ ps. Individual contributions of the slip facets to this integral distribution are weighed by each facet's area. In Fig. 3c-d the distribution of slip normals is plotted in equi-rectangular projection

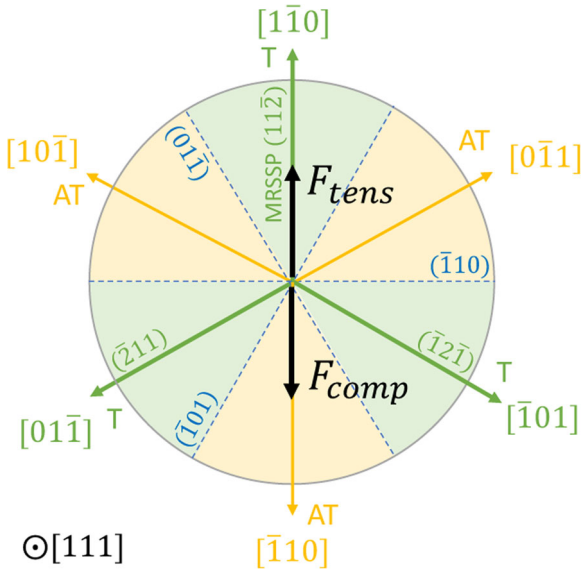

Fig. 2 Crystallographic directions and planes relevant for the motion of $\frac{1}{2}[111]$ dislocations. The $\frac{1}{2}[111]$ zonal vector is pointing out towards the viewer. The arrows show directions of the Peach-Koehler (PK) force acting on a right-hand screw $\frac{1}{2}[111]$ dislocation under compression ($\boldsymbol{F}_{\text{comp}}$) and tension ($\boldsymbol{F}_{\text{tens}}$) along the [001] axis. In both cases the PK force is parallel to the vertical (11$\bar{2}$) slip plane, referred to as the maximum resolved shear stress plane (MRSSP)

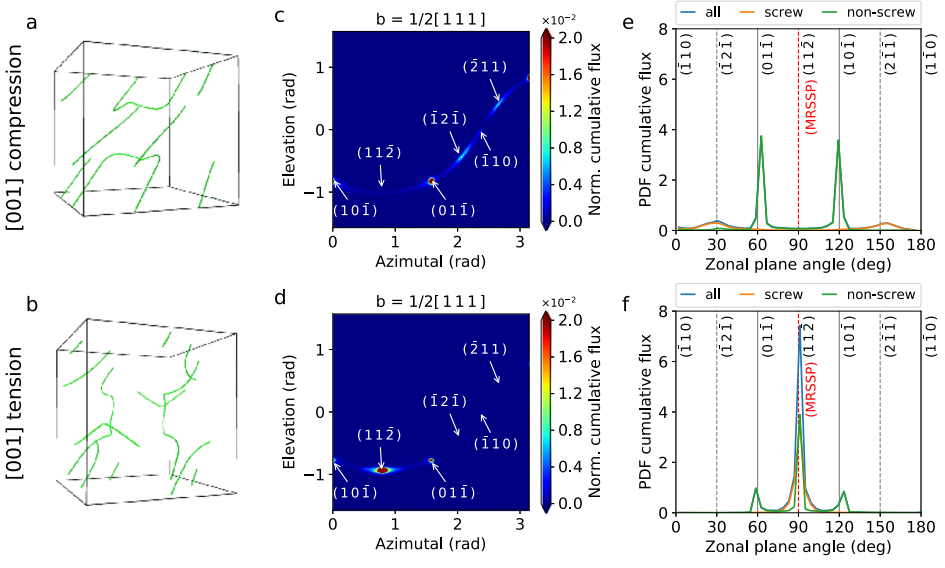

Fig. 3 Slip behavior of a single $\frac{1}{2}[111]$ prismatic loop introduced into an otherwise perfect crystal of BCC Ta and subjected to uniaxial compression or tension along the [001] axis. **a**–**b** DXA snapshots of the dislocation configurations attained after $t = 200$ ps under **a** compression and **b** tension. **c**–**d** Maps of dislocation flux extracted from STA facets accumulated from time $t = 0$ to $t = 400$ ps under **c** compression and **d** tension. The maps are the equi-rectangular (geographic) projections of the cumulative distribution over the hemi-sphere of the slip facet normals $\{\Delta\boldsymbol{A}^i\}$ (i.e. effective slip planes). Contribution of each facet $\Delta\boldsymbol{A}^i$ to the slip plane orientation statistic is weighted by the facet's swept area or incremental flux $\Delta\gamma^i = \Delta A^i \|\boldsymbol{b}^i\|/V$. **e**–**f** Probability distribution of the cumulative flux as a function of the [111] zonal plane angle and dislocation character under **e** compression and **f** tension

(i.e. geographic projection most commonly used in plotting world maps) as a function of the elevation (latitude) and the azimuthal angle (longitude) both given in radians. Because facets with normals $[hkl]$ and $[\bar{h}\bar{k}\bar{l}]$ correspond to slip on the same crystallographic plane (hkl), it is sufficient to map this and other similar distributions over a hemi-sphere. The projection is oriented so that the set of vectors zonal (perpendicular) to the $\frac{1}{2}[111]$ Burgers vectors traces one half of a full sinusoid on the map. To correct for area distortion specific to this geographic projection, contribution of each facet normal to the cumulative distribution was additionally weighed by the sine of its latitude angle. Density of the slip facet distributions is expressed in the color scale shown on the right side of each map. On Fig. 3e–f the same cumulative distributions are presented as functions of the dihedral (zonal) angle between the facet plane and the reference $(\bar{1}10)$ plane of the [111] zone (horizontal plane in Fig. 2). On the last two plots the flux is further partitioned into its screw and non-screw components counting as screw all dislocation segments with the character angles $\theta < 20^\circ$ (where θ is the angle between the segment line direction and its Burgers vector).

The STA data presented in Fig. 3 shows how T/AT asymmetry manifests itself in the motion of dislocation lines composing the loop. In both cases, the loop is oriented with respect to the [001] straining axis so as to induce slip of four out of six edge segments in the $(01\bar{1})$ and $(10\bar{1})$ planes. And indeed, this is precisely what happens as soon as straining commences: edge segments in each of two active slip planes begin to move in the opposite directions making the loop rotate. At the same time, the remaining two inactive segments in the $(1\bar{1}0)$ plane gradually align with the loop's Burgers vector drawing into two long screw dislocations. The loop rotates in the opposite directions under tension and compression because of the different sign of the resolved shear stress. Appearance of slip in the {112} planes is a clear indication that the newly drawn screw dislocations glide into {112} planes both under compression, Fig. 3e, and under tension, Fig. 3f. (Note that the initial edge segments of the loop are confined to glide on their {110} planes). However, relative contribution of {112} slip to the accumulated plastic flux and, most importantly, in which particular {112} planes such slip is taking place, are markedly different in tension and compression.

Under tension two freshly drawn screws glide right away on the $(11\bar{2})$ MRSSP which is reflected in the large peak around the $(11\bar{2})$ MRSSP in Fig. 3f. This is accompanied by glide of non-screw dislocations that follow the screws into the same MRSS plane. Two smaller peaks on the same plot near the $(01\bar{1})$ and $(10\bar{1})$ planes correspond to the initial expansion of the active edge segments of the prismatic loop, however much of subsequent slip takes place in a narrow interval of zonal angles near the MRSSP. Under compression, the drawn screws remain immobile and straight while the remaining non-screw segments continue to glide thus accumulating substantial amount of slip in two active {110} planes. Eventually, on reaching still higher stress, the screws begin to glide but, rather than gliding on the MRSSP, screw glide takes place on $(\bar{1}2\bar{1})$ and $(2\bar{1}\bar{1})$ planes less favorably aligned for slip (their Schmid factors are 0.235 which is only half of that on the MRSSP, at 0.47), as attested by two small peaks around these two planes in Fig. 3e. Dislocations glide under compression is overall insufficient to continue to relieve stress and an altogether different mechanism of stress relief – twinning – is triggered once uniaxial strain approaches ~ 0.4 (see Zepeda-Ruiz et al. (2017) for details of twinning transition in the same model of tantalum).

Tension/compression asymmetry in large-scale MD simulations of bulk crystal plasticity

Having examined crystallography of dislocation slip originating from a single initial loop, we now apply our STA algorithm to see how individual dislocations move under tension and compression when immersed in a statistically representative ensemble of interacting dislocations. In order to simulate dislocation plasticity in the bulk, we followed the methodology described in (Zepeda-Ruiz et al. 2017) and seeded initial dislocations into the crystal in the form of three hexagon-shaped prismatic loops of 15 nm radius for each of the $\frac{1}{2}\langle 111\rangle$ Burgers vectors (i.e. 12 loops in total). The loops were randomly positioned in the simulation volume containing about $2^{25} \sim 33$ million atoms, with initial dimensions of 66nm $\times$ 66nm $\times$ 135nm in compression, and 106nm $\times$ 106nm $\times$ 53nm in tension.

Asymmetry in the stress-strain response

Stress-strain response and dislocation density evolution observed under tension and compression in our bulk MD simulations is presented in Fig. 4. Consistent with experimental observations (Byron and Hull 1967; Hull et al. 1967; Sherwood et al. 1967; Webb et al. 1974), the simulated flow stress and dislocation density curves reveal a clear asymmetry with respect to the loading direction. We note however that, while asymmetry in yield response to tension and compression along the [001] axis is well established, experimental data on tantalum is conflicting. For instance, Sherwood et al. (1967) report higher yield stress under [001] compression in single-crystal Ta compared to tension at low temperatures with any such asymmetry vanishing at room temperature. On the other hand, Byron and co-workers (Byron and Hull 1967; Hull et al. 1967) report the opposite, with a higher yield stress observed under [001] tension compared to compression at 300K. In our MD simulations, both the flow stress and the dislocation density attained under compression are markedly higher than under tension. Our results are also consistent with an extensive study of Argon and Maloof (1966) who examined flow stress asymmetry by performing

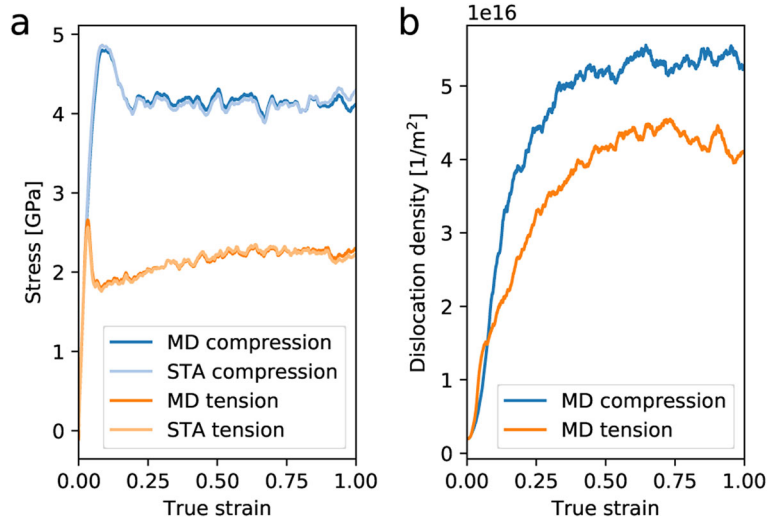

Fig. 4 **a** Comparison of MD and STA stress-strain curves for bcc Ta strained along the [001] axis in compression and in tension at a strain rate of $\dot{\varepsilon} = 2 \times 10^8$ /s. The STA stress-strain curves are reconstructed from slip facet data computed using the STA algorithm after which a 3% systematic correction is applied. **b** Evolution of dislocation densities ρ extracted from DXA snapshots of the same two simulations

sequences of [001] tension/compression cycles in single-crystal Ta in the temperature range 77K-450K. While still puzzling, we observe that nearly all cited experimental data pertains to T/C asymmetry in the yield stress which is known to depend on initial (pre-deformation) dislocation microstructure. In our simulations, the initial microstructures – prismatic loop sources – were exactly the same prior to tension and compression. Furthermore, as was shown in (Zepeda-Ruiz et al. 2017), after sufficiently large plastic strain ($\sim 0.4 - 0.5$ of true strain), all memory of initial dislocation microstructure in MD simulations is wiped off and both the flow stress and the dislocation density attain a state of steady flow in which they remain for as long as straining conditions remain constant. Thus, we consider our results on the steady flow stress to be representative of intrinsic material response independent of details of sample preparation. We further note that a similar T/C asymmetry has been observed in BCC metals other than tantalum which suggests that this asymmetry is generic to all BCC metals and ultimately originates in the particular geometry of the BCC lattice (Christian 1983).

To verify our STA approach, we first compare net plastic strain produced in our MD simulations with the same plastic strain computed by summing over plastic strain increments associated with each slip facet extracted during the same simulations. The STA method can be considered accurate to the extent that these two measures of plastic strains are equal. The axial zz component of the plastic rate tensor at time t must be equal to the following sum over slip facets computed by reconnecting two DXA snapshots extracted at times t and $t + \Delta t$:

$$\dot{\varepsilon}^p_{zz} = \frac{\Delta \varepsilon^p_{zz}}{\Delta t} = \frac{1}{\Delta t\, V} \sum_i \Delta A^i_z\, b^i_z \tag{3}$$

Total plastic strain attained at time t should be equal to the time integral of the above expression over all slip facets produced by the same time t. Expressed as a function of total strain, the flow stress should be equal to

$$\sigma_{zz}(\varepsilon_{zz}) = E \int_0^{t(\varepsilon_{zz})} \left(\dot{\varepsilon} - \dot{\varepsilon}^p_{zz}\right) dt \tag{4}$$

The above expression reconstructs flow stress σ_{zz} from instantaneous plastic strain rate $\dot{\varepsilon}^p_{zz}$ obtained as a sum over all slip facets computed over time interval Δt. Here, V is the simulation volume, $E = 119.26$ GPa is the Young's modulus for the [001] straining direction and $\dot{\varepsilon} = 2\times10^8$/s is the constant straining rate maintained along the z axis. To exclude initial transient plasticity, we first computed $\dot{\varepsilon}^p_{zz}$ and integrated the resulting strain rates over simulation time interval from $t = 1.25$ ns to $t = 3.75$ ns over which total strain increases from 0.25 to 0.75. The resulting reconstructed plastic strain is 0.515 in compression and 0.487 in tension, which are both within 3% of 0.5. After applying a systematic 3% correction to the values of $\dot{\varepsilon}^p_{zz}$, the entire stress-strain curves reconstructed from the STA data using Eq. (4) are compared to the MD curves in Fig. 4. The agreement with the MD results is very close: the reconstructed and the actual stress-strain curves nearly overlap and the reconstructed curves closely track time sequence of the actual stress fluctuations. Figure 4 verifies consistency of our STA algorithm and confirms that every detail of macroscopic stress-strain response can be ultimately traced to the underlying motion of dislocations.

The stress-strain curves in Fig. 4a show clear T/C asymmetry with both yield and flow stress under compression markedly higher than under tension. Similar but much less pronounced asymmetry is evident in the dislocation density-strain plots in Fig. 4b, with the dislocation density attained under compression higher than under tension. We note that, within the standard Taylor hardening equation relating resolved shear stress to the square root of dislocation density, the moderately higher dislocation density attained under compression is clearly insufficient to explain the much higher flow stress: the ratio of square roots of two dislocation densities is ~ 1.1 whereas the ratio of two flow stresses is ~ 1.8. Taylor hardening correspondence is improved if the shear stress is computed by projecting the axial stress on two inclined {112} planes stressed in the T sense under compression rather than projecting on the MRSSP as is appropriate for tension. In the latter case, because the Schmid factors of the two inclined {112} planes are precisely half that of the MRSSP, the same Taylor hardening equation yields 2.2 for the ratio of flow stress under compression to the flow stress under tension.

Asymmetry in crystallographic slip

Having earlier observed that memory of initial dislocation sources persists to rather substantial strains, to exclude such transients and to analyze intrinsic crystallography of dislocation motion we show in Fig. 5a-b the integral statistics of slip facet normals computed on every pair of dislocation networks over the interval of true strains from 0.5 to 1.0. Normals of slip facets traced by dislocations moving by conservative glide should be strictly confined to the planes of the four Burgers vector zones and thus should fall on the four sharp sinusoids on our equi-rectangular maps. The actual STA facet normals appear to be spread over a finite interval of ~ 2 to 4 angular degrees around the zonal sinusoids

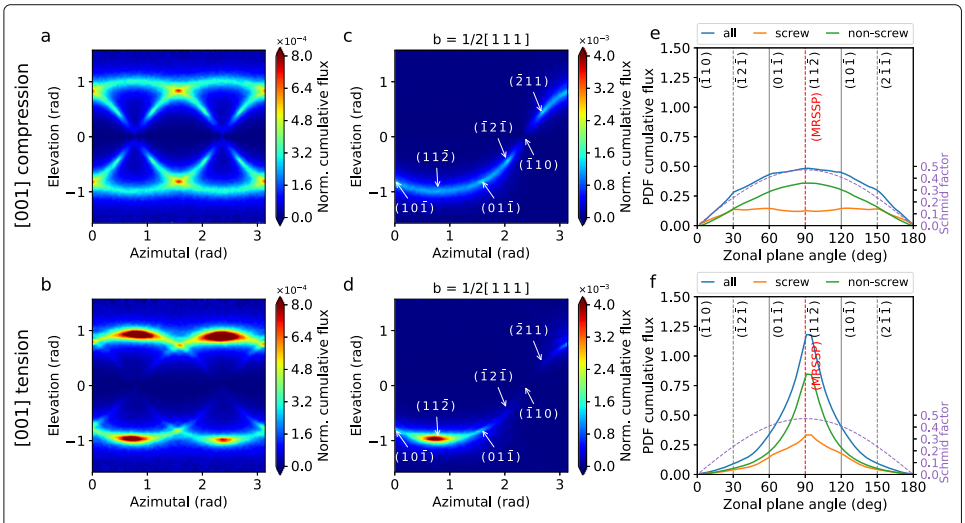

Fig. 5 Slip maps of dislocation motion under [001] uniaxial compression and tension during simulations of bulk plasticity. **a**–**b** Maps of the cumulative dislocation flux γ from all dislocations from strain 0.5 to 1. **c**–**d** Maps of the cumulative dislocation flux from the $\frac{1}{2}[111]$ dislocations alone. Positions of relevant crystallographic slip planes along the [111] zone are indicated. **e**–**f** Probability distribution of slip facets area as a function of the ⟨111⟩ zonal plane angle for all $\frac{1}{2}\langle 111\rangle$ dislocations. The flux is further partitioned into screw and non-screw dislocations contribution, where non-screw dislocations correspond to facets with character angle $\theta \geq 20°$. The thin dashed line is the Schmid factor variation over the zone with its scale shown on the right axis

which is likely to reflect finite accuracy of dislocation positioning in DXA and STA and/or local lattice rotations induced by dislocations.

Slip facet distributions observed under compression and under tension are again asymmetric, but not in the same way as in the previously discussed case of single loop. To reduce clatter, Fig. 5c-d shows the same statistics of slip facet orientations as in Fig. 5a-b but only for a 1/4 subset of slip facets associated with the $\frac{1}{2}[\,111]$ dislocations (distributions associated with the other three $\frac{1}{2}\langle 111\rangle$ Burgers vectors are similar by symmetry). Under tension (Fig. 5d), dislocation slip is again largely localized on and near the $(11\bar{2})$ MRSSP plane with the PK force pointing in the T direction (see Fig. 2). Even though under compression the MRSSP is just as perfectly aligned with the same $(11\bar{2})$ plane, the PK force now acts in the AT direction and, rather than gliding in the $(11\bar{2})$ MRSSP, slip activity becomes rather defuse, spreading with relatively constant intensity over a much wider range of plane orientations than under tension.

Figure 5e–f show slip facets distributions for all $\frac{1}{2}\langle 111\rangle$ dislocations as functions of the $\langle 111\rangle$ zonal plane angle and partitioned between screw and non-screw dislocation segments. Here the zonal angle is defined as the angle between the slip plane associated with each facet and a reference {110} plane (shown horizontal for $\frac{1}{2}[\,111]$ in Fig. 2) chosen for each Burgers vector so that an angle of 90° corresponds to slip on the {112} MRSSP. Here again, any segment with the character angle $\theta < 20°$ is counted as screw. Figure 5f shows that under tension both screw and non-screw dislocations glide predominantly on or near the {112} MRSSP. Under compression, the screws glide in still wider sectors of each Burgers vector zone showing slight enhancements of flux on two inclined {112} planes stressed in the T direction, and {110} planes. At the same time, glide of the screw dislocation on and around the MRSSP is relatively suppressed, Fig. 5e. When summed over all dislocation characters, the overall flux distribution shows a broad dome-shaped maximum centered on MRSSP quite similar to the fractional distribution associated with non-screw dislocations. By comparing our STA data in Fig. 5e–f, the tension/compression (or T/AT) asymmetry presents itself in marked differences in slip crystallography that are not limited to screw dislocations but involve all dislocation characters. Whereas under tension dislocations of all characters glide predominantly in a narrow zone around the {112} MRSSP, under compression the enhanced resistance to screw dislocation glide in the AT directions results in a relative depletion of screw characters near MRSSP and in a much wider distribution of dislocation flux over the planes of the Burgers vector zone.

The double dot product of the geometric Schmid tensor with the stress tensor is the Schmid factor m, a scalar measure of efficiency with which mechanical stress performs work on moving dislocations in a given slip system (slip system = {Burgers vector, slip plane}). The larger the Schmid factor the greater the PK force dislocations see from the applied stress. Thus, dislocations are expected to be more active – move faster and/or multiply at a faster rate – in slip planes with higher Schmid factors. As shown on the right axis in Fig. 5e, under compression flux distribution over all dislocation characters closely follows variations of the Schmid factor across the zone, thus corresponding to the often-hypothesized pencil (non-crystallographic) motion of dislocations: the amount of slip (swept area) produced in each slip plane of the zone is proportional to the plane's Schmid factor. Under uniaxial stress conditions imposed in MD simulations reported here, the same Schmid factor defines how much a unit of slip produced in a given slip system contributes to ε^{p}_{zz}, the component of plastic strain parallel to the straining axis. Under

definition of the zonal angle adopted in Fig. 5, the Schmid factor of a plane with angle ϕ is simply $\sin(\phi) * m_{\mathrm{MRSSP}}$ where $m_{\mathrm{MRSSP}} = 0.47$ is the maximum Schmid factor of the zone at $\phi = 90^\circ$ corresponding to the MRSSP plane. Taken over the zonal angle, the integrals of the product of the Schmid factor and the flux distributions shown in Fig. 5e-f provide a measure of relative efficiency in relieving external strain of dislocation motion under tension and under compression. The so-averaged integral efficiency is 0.42 under tension and 0.37 under compression. This is in close agreement with the ratios of the imposed straining rate to the total (integral) dislocation flux observed in Fig. 6a in our MD simulations under tension and compression. That the so-defined slip efficiency approaches its geometric maximum for the zone $m_{\mathrm{MRSSP}} = 0.47$ indicates that under tension dislocations move on and very close to the MRSSP. The lower slip efficiency of 0.37 under compression corresponds to a hypothetical crystal in which all dislocations glide only in planes inclined at an angle of approximately 38 degrees to the MRSSP. Of course this does not mean that dislocations glide "somewhere between" the {110} and {112} planes inclined to MRSSP, but is a consequence of the pencil character of dislocation slip under compression. As another check on consistency of the STA algorithm, the ratio of the imposed straining rate to the integral dislocation flux projected on the straining axis (i.e. the plastic strain) is also shown on Fig. 6a. As expected, both under tension and under compression the flux projected on the straining axis rapidly converges to the imposed straining rate $\dot{\varepsilon}$ indicating that, except for relatively brief initial yield transients, the externally imposed strain is fully accommodated by dislocation slip (Zepeda-Ruiz et al. 2017). Overall, our STA data shows that glide of non-screw dislocations contributes relatively more to dislocation flux and to the net crystal plasticity (see Fig. 5e–f) which is further confirmed by noting that the ratio of screw to non-screw flux remains relatively stable and oscillates around $\sim$0.55 under both tension and compression, Fig. 6b.

Asymmetry in dislocation microstructure and dislocation velocities

Along with slip crystallography, we observe noticeable differences in dislocation microstructure under tension and compression. Figure 6c shows dislocation density partitioned over screw and non-screw populations as a function of strain. One signature of the T/C asymmetry is that the total dislocation density is higher in compression than in

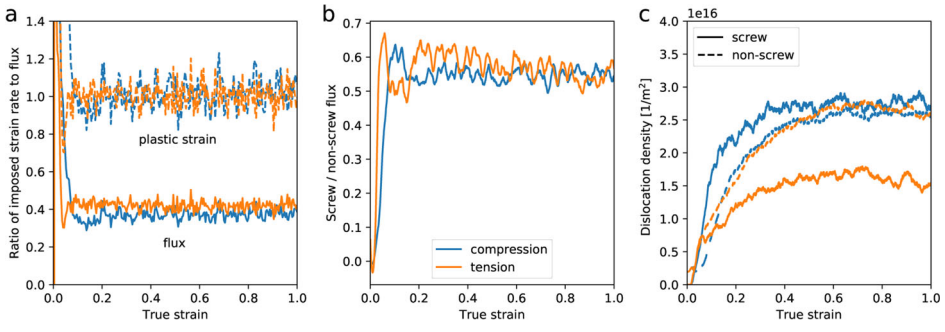

Fig. 6 In all panels curves pertaining to tension are shown in orange and curves pertaining to compression are shown in blue. **a** Ratio of the imposed straining rate to the total dislocation flux $\dot{\varepsilon}/\dot{\gamma}$ (solid lines) and ratio of the rate of plastic strain accumulation to the imposed straining rate $\dot{\varepsilon}/\dot{\varepsilon}^{p}_{zz}$ (dashed lines). **b** Ratio of the flux due to screw dislocations to the flux due to non-screw dislocations. (**c**) Densities of screw (solid lines) and non-screw (dashed lines) dislocations as functions of strain

tension (Fig. 4b) and that all of the difference is attributed to the screw sub-population, Fig. 6c. Although the quantities plotted on this figure depend on our somewhat arbitrary partitioning of dislocation segments into screw and non-screw sub-populations, other definitions for the screw/non-screw partitioning lead to qualitatively similar results: screw dislocations are more numerous than non-screws and the difference is greater under compression.

STA computes unit slip facets from two snapshots of the dislocation network separated by Δt. As defined in Fig. 1a, each slip facet contains information about the distance its segment moves over time Δt and retains information on the segment's length thus making it straightforward to compute the segment's velocity (averaged over Δt). A few statistical measures of dislocation velocity distribution computed on our MD simulation data are presented in Fig. 7. Positions of initial peaks in the average dislocation velocity (partitioned over screw and edge sub-populations) coincide with the peaks on the corresponding stress-strain curves (compare to Fig. 4a). Past the initial yield peaks, average velocities gradually decrease and approach their asymptotic values at a rate similar to the relaxation rate of the dislocation density (compare Fig. 7a-b to Fig. 4b). By comparison, as was first noted in (Zepeda-Ruiz et al. 2017), the flow stress relaxes to its stationary level at a faster rate (Fig. 4a), especially under compression. Another pertinent observation is that, initially reaching ~ 12 at yield under compression and ~ 6 under tension, past yield the ratio of edge to screw dislocation velocities gradually descends to much lower levels, Fig. 7c. These observations point to a scenario in which, as is commonly assumed, the yield stress is indeed defined by a high intrinsic lattice resistance to the motion of screw dislocations (at moderate temperatures). Flow stress past yield is increasingly defined by a

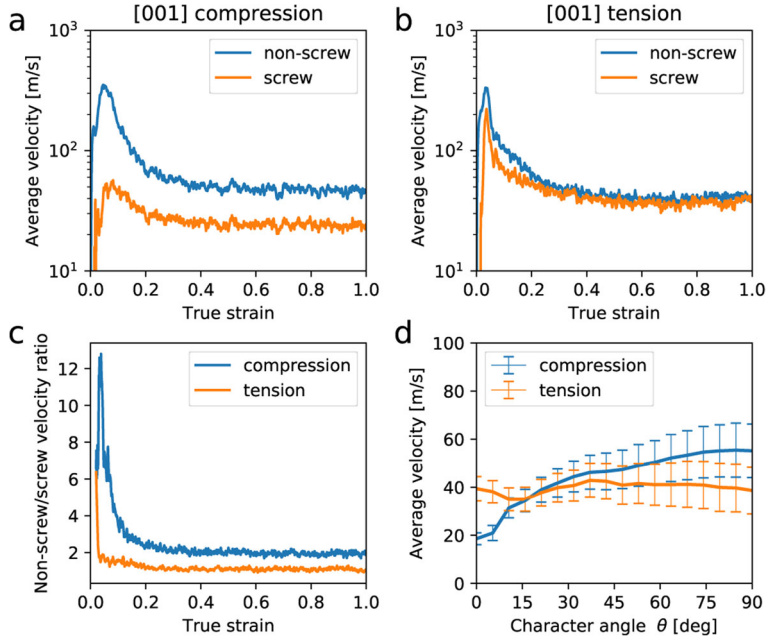

Fig. 7 Average velocities $\tilde{v}$ of screw and non-screw dislocation populations extracted from STA facets computed under uniaxial **a** compression and **b** tension. **c** Ratio of average velocity of non-screw dislocations to average velocity of screw dislocations as a function of strain. **d** Dislocation velocities averaged over strain interval from 0.5 to 1.0 broken down dislocation character angle

growing network resistance to dislocation motion to such an extent that in the steady flow regime under tension screw and edge dislocations move at nearly the same average velocities. And while the screws remain slower than the edges under compression, the ratio of edge/screw velocities goes down from ~ 12 at peak to ~ 2 in the steady flow. To avoid ambiguities due to the mentioned dependence of quantitative results on our specific convention for screw/edge partitioning, Fig. 7d shows the same statistics over the entire range of dislocation character angles accumulated over strain interval from 0.5 to 1.0 which excludes the initial yield transients. While the average velocities seem to be relatively uniform across character angles under tension, dislocations of near-screw characters remain markedly slower under compression.

Figure 8 shows the breakdown of dislocation links by their contribution to the overall plastic strain. Here a link is defined as a dislocation line connecting two network nodes (Sills et al. 2018). Although related to the segment velocity distributions discussed above, links are different objects typically consisting of multiple segments of varying characters. Unlike segment mobility data in Fig. 7 pertaining to mobility of dislocation segments of different characters, breakdown by links is focused on the network aspects of dislocation motion. Figure 8a shows cumulative contribution to plastic strain of all links integrated from the lowest to the highest contributors. If every link were to contribute an equal plastic strain, this cumulative function would follow the straight dashed line drawn in the

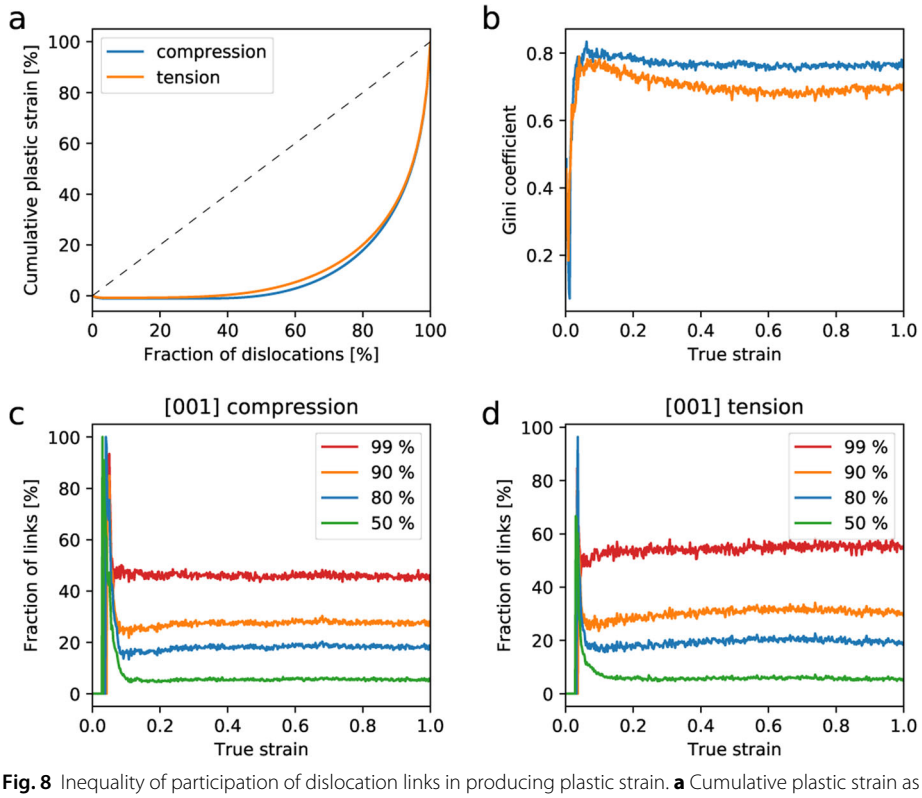

Fig. 8 Inequality of participation of dislocation links in producing plastic strain. **a** Cumulative plastic strain as a function of the fraction of dislocation links ordered from the lowest to the highest contributor. The dashed line corresponds to equal participation. **b** Evolution of the Gini coefficient under compression and tension. **c**–**d** Evolution of percentile contributions to plastic strain under compression (**c**) and tension (**d**): each line shows the fraction of highest contributor links responsible for a certain percentile of plastic strain, plotted as functions of strain

figure. Instead, both under tension and under compression on average about 40% of all links contribute virtually nothing to the net plastic strain. Above 40%, contribution of links to plastic strain grows increasingly rapidly with top 5% contributing 50% of the net plastic strain. To quantify inequality among individual link's contributions to crystal plasticity, we use the Gini coefficient commonly used in socio-economic contexts (Dorfman 1979). The Gini is equal to the fraction of the area of the triangle enclosed between the inclined dashed line and the cumulative distribution curve: the Gini is zero in the limit when all links contribute equally and is one in the limit when only the highest contributing links produce all the strain. Here the Gini coefficient is calculated as (Dorfman 1979):

$$G = \frac{\sum_{i=1}^{n} \sum_{j=1}^{n} \left| \varepsilon_i^p - \varepsilon_j^p \right|}{2n^2 \, \bar{\varepsilon^p}} \tag{5}$$

where ε_i^p is the plastic strain produced by link i over time interval Δt, $\bar{\varepsilon^p}$ is the average plastic strain generated by all links during the same time interval, and n is the total number of links. The Gini coefficients computed along our two straining trajectories are plotted in Fig. 8b as functions of strain. During the initial transients both under tension and compression all dislocations pre-seeded in the form of prismatic loops move quickly and evenly resulting in a low Gini coefficient. Then after reaching their peaks at strains close to the upper yield points, both Ginis gradually decrease to their steady values of 0.76 (compression) and 0.69 (tension). For reference, Gini values characterizing income inequality among countries of the world range between 0.2 (relative equality) and 0.6 (extreme inequality). The very high Gini's observed in our MD simulations suggest "extreme inequality" among the links in their contribution to crystal plasticity, the inequality more extreme under compression than under tension.

Another common way to represent inequality is in percentiles. In Fig. 8c–d we plot the fraction of top contributor links responsible for a given percent of plastic strain. The plots again show that about 5% of the most active dislocation links produce 50% of the net plastic strain (green) while 99% of plastic strain is produced by roughly half of all links (red) with the remaining links contributing only about 1%. Although some of the so-quantified inequality can be related to differences in link lengths (Sills et al. 2018), most of it reflects that only a small fraction of active links is moving appreciably at any instant of time while the rest of the links stays relatively motionless. This behavior is well captured in the STA snapshots in Fig. 1c-d (notice unequal widths of slip surfaces depicted in blue) and is consistent with a "stop-and-go" character of dislocation motion often assumed in strain-hardened metals in which dislocations spend most of their time waiting at obstacles, e.g. dislocation junctions, and only on occasion breaking away and moving fast only to be tied up again at yet another obstacle. Remarkably, we observe the same behavior under extremely high straining rates, at the very limit where dislocations can still accommodate plastic straining.

Discussion and conclusion

STA data presented in the preceding sections directly connects tension/compression asymmetry in plasticity response of tantalum to an underlying T/AT asymmetry of dislocation motion in BCC crystals. In our high-rate MD simulations of uniaxial straining along the high-symmetry [001] axis, most slip activity of screw dislocations occurs on and near the {112} MRSSP planes under tension. Under compression screw dislocations

glide in much wider sectors of glide planes with minor enhancements of slip activity at the {112} and {110} planes inclined at angles to the MRSSP. Similar asymmetry is observed in the motion of non-screw dislocations that glide at and near MRSSP under tension while gliding in all zonal planes under compression. When integrated over all dislocation characters, dislocation slip is crystallographic (largely confined to the {112} MRSSP) under tension and pencil (distributed all over the ⟨111⟩ zones) under compression. The asymmetry is rationalized by observing that dislocation glide in the {112} planes is easy in the twinning directions whereas glide of the screw dislocations in the anti-twinning sense is difficult. Given that each Burgers vector zone has three twinning directions at 120° angles with each other, the sense of dislocation glide – twinning or anti-twinning – is inverted from tension to compression. Thus, selection of active slip systems in BCC tantalum is based not only on the magnitude of their Schmid factors, but also on the Schmid factor's signs with respect to the twinning directions of dislocation glide.

Our approach to elucidating origins of tension/compression asymmetry of the flow stress in BCC metals differs from prior work focused on the behavior of a single screw dislocation in an atomistic model (Ito and Vitek 2001; Vitek 2004; Dezerald et al. 2016; Kraych et al. 2019). Here, our large-scale MD simulations present a unique opportunity to investigate the same behaviors in silico, using a combination of DXA and STA analyses, in large statistically representative dislocation ensembles fully accounting for interactions among dislocations of all characters, screw and non-screw alike.

Observations of dislocation slip reported in this study are largely consistent with experimental results. In (Sherwood et al. 1967), {112} slip was observed under [001] tension (along with some twinning at 77K) while deformation was reported to proceed on {110} planes under compression. Similar results where observed in (Byron and Hull 1967; Hull et al. 1967), where the operating slip planes in tension were seen to be those aligned with the MRSSP, while in compression greater deviations from the MRSSP towards {110} planes were observed. Recently, dislocation motion in {112} planes in the twinning sense was observed in *in situ* TEM experiments on single crystal tungsten subjected to tensile loading while, at the same time, no motion in {110} planes was observed (Caillard 2018). {112} slip at moderate temperatures was also recently observed experimentally through scanning tunneling microscope in niobium crystals (Douat et al. 2019), where the manifestation of the T/AT asymmetry and pencil (non-crystallographic) slip were clearly confirmed in the slip trace statistics. At the same time, our observations do not fully agree with the predominance of {112} glide in tantalum single crystals reported very recently based on data of quasi-static and dynamic compression experiments (Lim et al. 2020). By analyzing slip traces observed in single crystal tantalum subjected to compressive straining and comparing their experimental results with crystal plasticity finite element calculations, the authors concluded that ⟨111⟩{112} glide was the dominant mechanism of crystal plasticity under compressive loading.

To assess robustness of our results and observations on tantalum, we repeated the same two large-scale MD simulations using two other EAM inter-atomic potentials developed for BCC tungsten in (Juslin and Wirth 2013) and for BCC iron in (Mendelev et al. 2003). Just as in tantalum, robust tension/compression asymmetry in the yield and flow stress response is observed in tungsten and iron. Furthermore, subsequent STA analyses revealed qualitatively identical asymmetry in slip crystallography and dislocation microstructure. It was previously suggested that dislocation glide in {112} planes often

observed in MD simulations is as a consequence of the known tendency of some interatomic potentials to predict a wrong (degenerate) core structure for the screw dislocation (Chaussidon et al. 2006), or the presence of metastable split core structures (Hale et al. 2014). We observe that {112} slip of screw dislocations under tension dominates in all three interatomic potential models employed in our MD simulations two of which (Ta and α-Fe) are known to predict correct (non-degenerate) core structure. Factoring in the {112} slip predictions obtained with *ab-initio* calculations in Ta (Woodward and Rao 2002; Segall et al. 2003) and the recent experimental observations mentioned in the above (Lim et al. 2020), we thus believe that, irrespective of accuracy or inaccuracy of the interatomic potentials, twinning/anti-twinning induced asymmetry of slip crystallography is the root cause of tension/compression asymmetry in macroscopic crystal plasticity of BCC metals.

In conclusion, we developed a practical computational method for extracting details of dislocation motion from large-scale simulations of crystal plasticity. Our new sweep-tracing algorithm (STA) tracks dislocation motion by reconnecting successive dislocation configurations generated in mesoscale DDD simulations or extracted from MD simulations using the DXA algorithm. STA relies on point-wise matching of Nye's tensor fields of two dislocation networks to sidestep difficulties associated with pairing dislocation networks of differing topology and line discretization. As its first application, STA is applied to elucidate the nature of the notorious tension/compression asymmetry commonly observed in BCC metals. Taking in as its input a sequence of dislocation networks extracted from large-scale MD simulations of tantalum, tungsten, and iron, we used STA to compute and collect statistics of unit slip facets swept by dislocation segments which provide a wealth of information on the character of dislocation motion including slip crystallography. Based on this data, we report that under uniaxial tension dislocations glide primarily on the {112} MRSSP in the twinning direction. In contrast, under compression dislocation glide is non-crystallographic/pencil with slip activity tightly correlated with the Schmid factor and widely distributed over planes of the $\langle 111 \rangle$ zones. Tension/compression asymmetry is directly related here to the observed refusal of screw dislocations to glide in the {112}AT directions under compression thus supporting the long assumed direct relationship between macroscopic tension/compression asymmetry and crystallographic T/AT slip asymmetry in BCC metals. Thus, our observations directly link details of dislocation motion at the atomic scale to the resulting mechanical response at the macroscopic scale.

In tandem with the widely used DXA algorithm, STA constitutes an accurate and efficient computational method for gaining new insights and for extracting quantitative information on the dynamics of dislocation motion from massive DDD and MD simulations of crystal plasticity. In this capacity STA provides a valuable tool for addressing the growing challenge of dealing with immense amounts of numerical data generated in such simulations.

Appendix

A Numerical implementation of the STA algorithm

In this section we provide additional details regarding the numerical implementation of the STA algorithm. Given two input dislocation networks $\mathcal{N}_t$ and $\mathcal{N}_{t+\Delta t}$ at times t and $t+\Delta t$, the algorithm starts by computing their Nye's field representation, Eq. (1). Numerically, this is done following the approach introduced in (Bertin 2019). Specifically, for a

given network, the discrete dislocation tensor at grid point $\boldsymbol{x}^d$ is calculated as:

$$\alpha_{ij}\left(\boldsymbol{x}^d\right) = \sum_{s}^{N_{\text{seg}}} b_i^s t_j^s \int_{L^s} S\left(\boldsymbol{x}^d - \boldsymbol{x}\right)\, dL(\boldsymbol{x}) \tag{6}$$

where the sum is performed over all segments $s = 1, ..., N_{seg}$ of the network and the line integral is carried along each segment L^s. $\boldsymbol{b}^s$ and the $\boldsymbol{t}^s$ are the Burgers vector and the unit tangent vector associated with straight segment s, respectively. $S(\boldsymbol{x}^d - \boldsymbol{x})$ denotes a weighting function associated with each grid point $\boldsymbol{x}^d$ that satisfies the partition of unity. Following (Bertin 2019), we use the Cloud-In-Cell (CIC) weighting scheme (Birdsall and Fuss 1969) whose three-dimensional expression is given by:

$$S\left(\boldsymbol{x}^d - \boldsymbol{x}\right) = \begin{cases} \prod_{i=1}^{3} \left(1 - \frac{\left|x_i^d - x_i\right|}{H_i}\right) & \text{when } \left|x_i^d - x_i\right| < H_i,\ \forall i \in \{1,2,3\} \\ 0 & \text{otherwise} \end{cases} \tag{7}$$

where H_i denotes the grid spacing in each spatial direction $i = \{1, 2, 3\}$. As shown in (Bertin 2019), the choice of this weighting function allows for an efficient, analytical evaluation of Eq. (6).

Once discrete Nye's tensor fields are evaluated using Eqs. (6)–(7), the distance between a pair of networks can be computed from their point-wise difference using Eq. (2). The task of reconnecting the two networks can now be regarded as an optimization problem that seeks to minimize the distance $E(\mathcal{N}_t, \mathcal{N}_{t+\Delta t})$ by taking advantage of the dual nodal/field representation of the networks. In our implementation this is solved using a gradient-descent method. Specifically, if one denotes $\{\boldsymbol{r}_t\}$ the set of all nodal positions of network $\mathcal{N}_t$, the reconnection $\mathcal{N}_t \rightarrow \mathcal{N}_{t+\Delta t}$ can be achieved by iteratively adjusting nodal positions $\{\boldsymbol{r}_t\}$ such as to minimize the networks distance:

$$\{\boldsymbol{r}_t^{i+1}\} = \{\boldsymbol{r}_t^i\} - \delta\, \boldsymbol{\nabla}_{\boldsymbol{r}_t} E\left(\mathcal{N}_t^i, \mathcal{N}_{t+\Delta t}\right) \tag{8}$$

where i is the iteration number, $\boldsymbol{\nabla}_{\boldsymbol{r}_t}$ denotes the gradient operator with respect to the nodal positions of network $\mathcal{N}_t^i$, and δ is a step size controlling the convergence rate. For convenience, the gradient vector is evaluated numerically by slightly perturbing the nodes around their current positions. To achieve an optimal convergence rate, an adaptative scheme is used to select the step size δ. Several trial values for δ (centered around the δ value determined at the previous iteration) are tested and the one that leads to the maximum distance reduction is selected. At each step i, the Nye's tensor field of intermediate dislocation network $\mathcal{N}_t^i$ is recalculated using Eqs. (6)–(7). If needed, an adaptive resolution scheme can be adopted whereby the discrete grid is being refined gradually during the iterative process. Convergence is achieved after a maximum number of iterations is reached or once the distance drops below a tolerance threshold, defined by user's demands on accuracy and available computational resource. Upon convergence, network $\mathcal{N}_t^{\text{conv}} = \tilde{\mathcal{N}}_{t+\Delta t}$ is obtained as a best approximant of the later network $\mathcal{N}_{t+\Delta t}$, and nodal displacements $\left\{\boldsymbol{r}_t^0\right\} \rightarrow \left\{\boldsymbol{r}_t^{\text{conv}}\right\}$ provides the effective trajectory of dislocation segments for time interval $[\,t, t + \Delta t]$.

The STA algorithm is efficient, easily parallelizable, and scales linearly with the number of nodes in the network, approximately with the cube root of the number of grid points used to evaluate the Nye's tensor (the number of voxels intersected by a line segment increases as $N^{1/3}$ when the total number of grid points N is increased), and linearly with

the number of iterations. As an example, for the MD configurations examined in this work we typically find that convergence is achieved in about 100 iterations. For a fully developed dislocation network with $\sim 20,000$ nodes (e.g. typical configurations from strain 0.5 to 1.0), this corresponds to CPU times of about 200, 300, and 450 seconds for grid resolutions $N = 16^3$, 32^3, and 64^3, respectively, using a single 3.0 GHz processor.

B Validation of STA algorithm against DDD simulations

Here we present a study of the effect of STA method parameters on the method's accuracy. Two main parameters need to be selected to fully define our STA algorithm, namely (i) time interval Δt between consecutive snapshots to be reconnected, and (ii) grid spacing s defining the resolution of the Nye's tensor field representation of the dislocation networks. Errors are inevitable at any combination of Δt and s but, since STA input is output of DXA, it is desirable to separate errors originating in the STA method itself from the ones passed on to STA from the preceding DXA analysis. While it may be possible to estimate DXA own errors, here we opted instead to use DDD simulations as a proxy method to generate dislocation networks for subsequent STA analysis. In DDD simulations dislocations consist of connected straight segments and the displacement of every such segment over every time step is known and can be recorded (Arsenlis et al. 2007). Thus, as a proxy to DXA, DDD simulations are error-free and comparing the "true" slip facets internally generated in DDD to the slip facet data computed using STA on the same DDD trajectory makes it possible to evaluate STA's own accuracy as a function Δt and s.

Here we exercise STA on a DDD simulation specifically designed to approximate as closely as possible our MD simulations. The simulation was performed using the DDD code ParaDiS (Arsenlis et al. 2007) in the same volume, under the same straining conditions and starting from the same 12 initial prismatic loops as in our MD simulations described in "Results" section. To make dislocations move as they do in MD, we used a linear pencil-glide mobility function appropriate for BCC metals (Arsenlis et al. 2007) calibrated against dislocation mobility data extracted from our own MD simulations of single screw and non-screw dislocations under the same interatomic potential of Li et al. (Li et al. 2003). Under compression along the [001] axis at the same rate $\dot{\varepsilon} = 2 \times 10^8$/s, the DDD simulation produced dislocation networks similar to those generated in MD. Setting the simulation time step of 10 fs (the same as in MD), we recorded the "true" slip facets and dislocation networks at every time step of the DDD simulation. Then, in order to examine how well STA output approximates the "true" DDD simulation data, we applied our STA algorithm to dislocations networks produced in DDD using several different combinations of Δt and s.

Figure 9a shows the stress-strain response obtained in the DDD simulation with the above described parameters but over a short time interval of 5000 time steps which corresponds to 0.01 increment in the axial strain (dashed red line). That both the flow stress, at $\sim$4 GPa, and the dislocation density, at $\sim 6 \times 10^{16}/\mathrm{m}^2$ (not shown), are close to the ones observed in the corresponding MD simulation confirms that the two models – DDD and MD – are indeed similar, as intended. Also shown on the same plot as thin lines of various colors are stress-strain curves reconstructed from STA slip facets computed from the DDD network snapshots using different choices for Δt and grid spacing $s \approx 5.3$, 2.6, and 1.3 nm which correspond to $N = 16^3$, 32^3 and 64^3 grid points along each dimension of the DDD simulation volume (see the legend). Reconstruction of these stress-strain curves

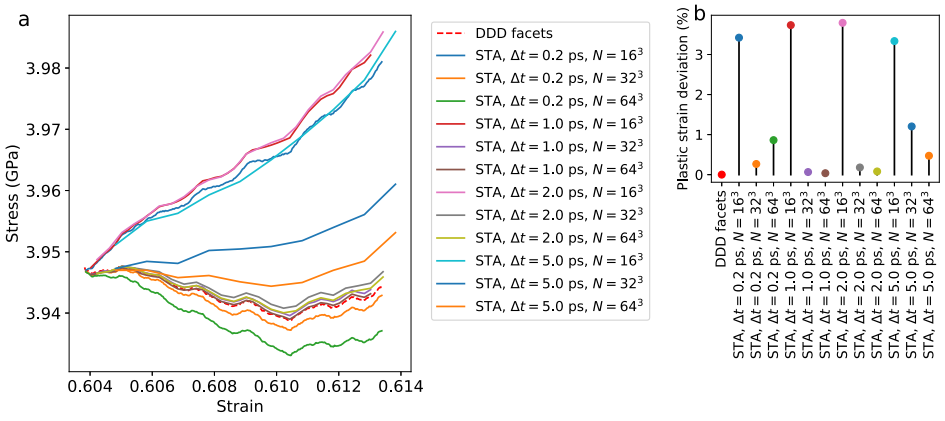

Fig. 9 Effect of the choice of STA parameters Δt and N on the accuracy of STA method when applied to a DDD simulation trajectory. **a** "Exact" stress-strain response from the DDD simulation (dashed red line) compared to stress-strain responses reconstructed from the STA facets obtained using various parameter values for Δt and N (see the legend). **b** Average deviation from the "exact" DDD plastic strain of plastic strain reconstructed from the STA facets extracted using different STA parameter values

was performed as described in "Asymmetry in the stress-strain response" section. Note that all reconstructed stress curves are close to the "exact" DDD result however, to zoom in on remaining discrepancies, we intentionally changed the scale of the stress axis. As seen from the curves, stress show largest divergence from the true stress response at all values of the STA interval Δt. STA facets extracted on finer grids $N = 32^3$ and $N = 64^3$ follow the true response much closer. Similar trend is obvious from Fig. 9b that shows for the same choices of Δt and N the average deviation of plastic strain computed from the STA facets from the "exact" plastic strain computed in the DDD simulation. Here again the coarsest grid $N = 16^3$ results in greatest average deviations. The smallest average deviations are obtained with $\Delta t = 1$ ps and grid resolutions $N = 32^3$ and 64^3, at 0.065% and 0.036%, respectively.

Figure 10a presents another test on the accuracy of our STA algorithm. Shown in the figure is the distribution over the zonal angle of the flux of $\frac{1}{2}\langle 111\rangle$ dislocations computed directly in the DDD simulation (exact flux distribution) and reconstructed from the STA facets extracted using different values of Δt and N (see "Tension / compression asymmetry in single-loop simulations" section for the definition of the zonal angle). It appears that flux distribution is well captured at all values of Δt and N, including its width reflecting the pencil character of dislocation mobility encoded in the mobility function used in the DDD simulations. The reconstructed STA flux distributions even reproduce the peaks in the true distribution possibly reflecting insufficient statistics of dislocation slip accumulated over the rather narrow interval of only 50 ps (= 5000 DDD time steps). Although greater deviations from the "true" flux distribution at coarser grids are again evident, these are more concisely summarized in Fig. 10b that shows the root mean square deviations (RMSD) from the exact DDD flux of the STA flux computed for the same sets of STA parameters. Again, STA flux computed with $\Delta t = 1$ ps and grid resolutions $N = 32^3$ and 64^3 shows the lowest RMSD. We note that the RMSD increases markedly when using the longest time interval of $\Delta t = 5$ ps which probably indicates excessive "warpage" of the slip facets resulting in a loss of accuracy in capturing crystallographic slip.

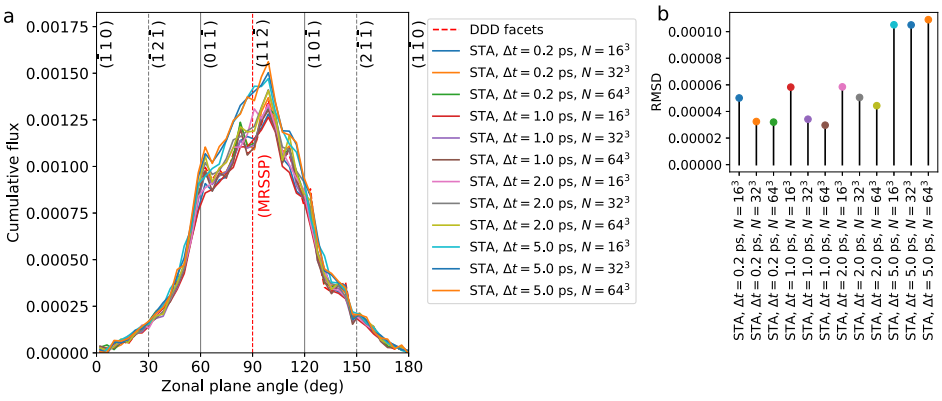

Fig. 10 **a** Dislocation flux as function of zonal angle (see legend and text for an explanation of colors). **b** Root mean square deviation (RMSD) from the "true" DDD flux of the zonal flux computed from STA facets using different STA parameters values

Results presented in this section demonstrate the ability of the STA algorithm to accurately reconstruct dislocations trajectories from network snapshots providing guidance for optimal selection of STA parameters for an intended application. Following the study discussed in this section, for our STA analysis of DXA data we opted for $\Delta t = 1$ ps and $N = 32^3$ as a set of STA parameters offering a reasonable trade-off between accuracy and cost of our DXA/STA workflow. Finally, It is worth noting that, when applied on DDD trajectories, the deviations of STA-reconstructed plastic strain from the exact DDD plastic strain for this parameter set are well below 1%. This is to be compared to the systematic deviation of $\sim$3% from the exact MD plastic strain observed with the same optimal set of STA parameters in "Results" section. This comparison suggests that the largest fraction of the total error of the DXA/STA workflow resides with the DXA method, likely owing to thermal fluctuations and other uncertainties in dislocation core positioning inherent to DXA.

Acknowledgements
The authors acknowledge numerous useful discussions with A. Stukowski.

Authors' contributions
NB developed and implemented the method. NB and LZR ran the MD simulations. NB and VB analyzed the results and wrote the paper. All authors read and approved the final manuscript.

Funding
This work was performed under the auspices of the U.S. Department of Energy by Lawrence Livermore National Laboratory under contract DE-AC52-07NA27344.

Availability of data and materials
The data analyzed in the current work is available from the corresponding author on reasonable request.

Declarations

Competing interests
The authors declare that they have no competing interests.

Received: 12 June 2020 Accepted: 15 November 2021
Published online: 06 January 2022

References

A. Argon, S. Maloof, Plastic deformation of tungsten single crystals at low temperatures. Acta Metall. **14**(11), 1449–1462 (1966)

A. Arsenlis, W. Cai, M. Tang, M. Rhee, T. Oppelstrup, G. Hommes, T. G. Pierce, V. V. Bulatov, Enabling strain hardening simulations with dislocation dynamics. Model. Simul. Mater. Sci. Eng. **15**(6), 553–595 (2007)
N. Bertin, Connecting discrete and continuum dislocation mechanics: A non-singular spectral framework. Int. J. Plast. **122**(2019), 268–284 (2019)
C. K. Birdsall, D. Fuss, Clouds-in-clouds, clouds-in-cells physics for many-body plasma simulation. J. Comput. Phys. **3**(4), 494–511 (1969)
J. Byron, D. Hull, Plastic deformation of tantalum single crystals: I. the surface morphology of yield. J. Less Common Met. **13**(1), 71–84 (1967)
D. Caillard, Geometry and kinetics of glide of screw dislocations in tungsten between 95k and 573k. Acta Mater. **161**(2018), 21–34 (2018)
J. Chaussidon, M. Fivel, D. Rodney, The glide of screw dislocations in BCC fe: atomistic static and dynamic simulations. Acta Mater. **54**(13), 3407–3416 (2006)
J. Christian, Some surprising features of the plastic deformation of body-centered cubic metals and alloys. Metall. Trans. A. **14**(7), 1237–1256 (1983)
L. Dezerald, D. Rodney, E. Clouet, L. Ventelon, F. Willaime, Plastic anisotropy and dislocation trajectory in BCC metals. Nat. Commun. **7**(2016), 11695 (2016)
M. a.-S. Duesbery, V. Vitek, Plastic anisotropy in BCC transition metals. Acta Mater. **46**(5), 1481–1492 (1998)
R. Dorfman, A formula for the Gini coefficient. Rev. Econ. Stat. **61**, 146–149 (1979)
B. Douat, C. Coupeau, J. Bonneville, M. Drouet, L. Vernisse, L. Kubin, Atomic-scale insight into non-crystallographic slip traces in body-centred cubic crystals. Scr. Mater. **162**(2019), 292–295 (2019)
M. R. Garey, D. S. Johnson, *Computers and Intractability: a Guide to the Theory of NP-completeness*. (WH Freeman and Company, New York, 1979), p. 1979
L. M. Hale, J. A. Zimmerman, C. R. Weinberger, Simulations of BCC tantalum screw dislocations: why classical inter-atomic potentials predict {1 1 2} slip. Comput. Mater. Sci. **90**(2014), 106–115 (2014)
D. Hull, J. Byron, F. Noble, Orientation dependence of yield in body-centered cubic metals. Can. J. Phys. **45**(2), 1091–1099 (1967)
K. Ito, V. Vitek, Atomistic study of non-schmid effects in the plastic yielding of BCC metals. Phil. Mag. A. **81**(5), 1387–1407 (2001)
N. Juslin, B. Wirth, Interatomic potentials for simulation of he bubble formation in w. J. Nucl. Mater. **432**(1-3), 61–66 (2013)
A. Kraych, E. Clouet, L. Dezerald, L. Ventelon, F. Willaime, D. Rodney, Non-glide effects and dislocation core fields in BCC metals. NPJ Comput. Mater. **5**(1), 1–8 (2019)
Y. Li, D. J. Siegel, J. B. Adams, X.-Y. Liu, Embedded-atom-method tantalum potential developed by the force-matching method. Phys. Rev. B. **67**, 125101 (2003)
H. Lim, J. D. Carroll, J. R. Michael, C. C. Battaile, S. R. Chen, J. M. D. Lane, Investigating active slip planes in tantalum under compressive load: crystal plasticity and slip trace analyses of single crystals. Acta Mater. **185**(2020), 1–12 (2020)
J. Nye, Some geometrical relations in dislocated crystals. Acta Metall. **1**(2), 153–162 (1953)
M. Mendelev, S. Han, D. Srolovitz, G. Ackland, D. Sun, M. Asta, Development of new interatomic potentials appropriate for crystalline and liquid iron. Phil. Mag. **83**(35), 3977–3994 (2003)
S. Plimpton, Fast parallel algorithms for short-range molecular dynamics. J. Comput. Phys. **117**(1), 1–19 (1995)
D. Segall, A. Strachan, W. A. Goddard III, S. Ismail-Beigi, T. Arias, Ab initio and finite-temperature molecular dynamics studies of lattice resistance in tantalum. Phys. Rev. B. **68**(1), 014104 (2003)
P. Sherwood, F. Guiu, H. C. Kim, P. L. Pratt, Plastic anisotropy of tantalum, niobium, and molybdenum. Can. J. Phys. **45**(2), 1075–1089 (1967)
R. B. Sills, N. Bertin, A. Aghaei, W. Cai, Dislocation networks and the microstructural origin of strain hardening. Phys. Rev. Lett. **121**, 085501 (2018)
A. Stukowski, A triangulation-based method to identify dislocations in atomistic models. J. Mech. Phys. Solids. **70**(2014), 314–319 (2014)
A. Stukowski, K. Albe, Extracting dislocations and non-dislocation crystal defects from atomistic simulation data. Model. Simul. Mater. Sci. Eng. **18**(8), 085001 (2010)
G. L. Webb, R. Gibala, T. E. Mitchell, Effect of normal stress on yield asymmetry in high purity tantalum crystals. Metall. Trans. **5**(7), 1581–1584 (1974)
C. R. Weinberger, B. L. Boyce, C. C. Battaile, Slip planes in BCC transition metals. Int. Mater. Rev. **58**(5), 296–314 (2013)
V. Vitek, Core structure of screw dislocations in body-centred cubic metals: relation to symmetry and interatomic bonding. Phil. Mag. **84**(3-5), 415–428 (2004)
C. Woodward, S. Rao, Flexible ab initio boundary conditions: simulating isolated dislocations in BCC mo and ta. Phys. Rev. Lett. **88**(21), 216402 (2002)
L. A. Zepeda-Ruiz, A. Stukowski, T. Oppelstrup, N. Bertin, N. R. Barton, R. Freitas, V. V. Bulatov, Atomistic insights into metal hardening. Nat. Mater. **20**(3), 315–320 (2021)
L. A. Zepeda-Ruiz, A. Stukowski, T. Oppelstrup, V. V. Bulatov, Probing the limits of metal plasticity with molecular dynamics simulations. Nature. **550**(7677), 492 (2017)

Publisher's Note